Axial Confocal Tomography of Capillary-Contained Colloidal Structures

Shir R. Liber,[†] Ganit Indech,[†] Ernest B. van der Wee,[‡] Alexander V. Butenko,[†] Thomas E. Kodger,[§] Peter J. Lu,[||] Andrew B. Schofield,[⊥] David A. Weitz,[||] Alfons van Blaaderen,[‡] and Eli Sloutskin[*,†]

[†]Physics Department and Bar-Ilan Institute of Nanotechnology & Advanced Materials, Bar-Ilan University, Ramat-Gan 5290002, Israel

[‡]Soft Condensed Matter, Debye Institute for NanoMaterials Science, Utrecht University, Princetonplein 1, 3584 CC Utrecht, The Netherlands

[§]Physical Chemistry and Soft Matter, Wageningen University & Research, Stippeneng 4, 6708 WE Wageningen, The Netherlands

[||]Department of Physics and SEAS, Harvard University, Cambridge, Massachusetts 02138, United States

[⊥]The School of Physics and Astronomy, University of Edinburgh, Edinburgh EH9 3FD, U.K.

S Supporting Information

ABSTRACT: Confocal microscopy is widely used for three-dimensional (3D) sample reconstructions. Arguably, the most significant challenge in such reconstructions is posed by the resolution along the optical axis being significantly lower than in the lateral directions. In addition, the imaging rate is lower along the optical axis in most confocal architectures, prohibiting reliable 3D reconstruction of dynamic samples. Here, we demonstrate a very simple, cheap, and generic method of multiangle microscopy, allowing high-resolution high-rate confocal slice collection to be carried out with capillary-contained colloidal samples in a wide range of slice orientations. This method, realizable with any common confocal architecture and recently implemented with macroscopic specimens enclosed in rotatable cylindrical capillaries, allows 3D reconstructions of colloidal structures to be verified by direct experiments and provides a solid testing ground for complex reconstruction algorithms. In this paper, we focus on the implementation of this method for dense nonrotatable colloidal samples, contained in complex-shaped capillaries. Additionally, we discuss strategies to minimize potential pitfalls of this method, such as the artificial appearance of chain-like particle structures.
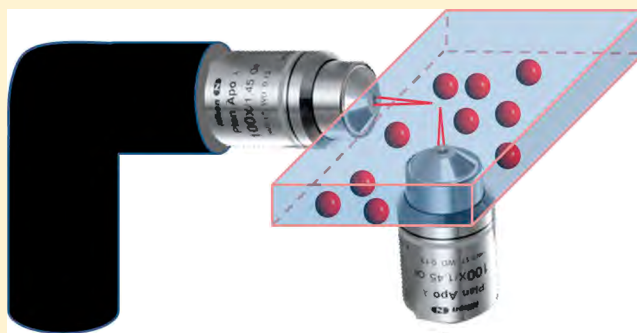
INTRODUCTION

Confocal microscopy is one of the central tools in modern soft condensed matter physics, chemistry, biology, and materials science.[1] The optical sectioning capabilities of confocal microscopy, with the spatial resolution within each slice approaching the diffraction limit, make full three-dimensional (3D) structural reconstructions possible, providing an unprecedentedly detailed insight into the physics of collective phenomena in colloidal suspensions[2,3] and resolving the full geometry of complex-shaped micro-objects,[4,5] such as the recently discovered faceted liquid emulsion droplets.[6] Typically, the individual optical cross sections are collected by scanning the fluorescently stained sample with (one or multiple) laser beams, exciting fluorophores. This in-plane scanning may be very fast, commonly carried out at supervideo rates. To take confocal sections at varying depths inside the sample, either the objective or the sample is translated along the optical axis. This on-axis scanning is typically slower and less accurate, limiting most confocal studies of dynamical systems to imaging of a single section normal to the optical axis; thus, the full 3D

information is only available for systems exhibiting relatively slow dynamics. In these quasistatic situations, a stack of optical slices is collected. A 3D reconstruction of such a stack commonly involves a 3D deconvolution, with the point spread function (PSF) used as a kernel. The PSF of the confocal microscopes is rotationally anisotropic: the resolution along the optical axis is typically lower by a factor of ∼3 compared to the other directions, along which the diffraction limit may be approached quite closely.[7] The PSF anisotropy challenges its precise deconvolution from the confocal data, complicates feature detection,[8−12] and limits the reliability of quantitative analysis based on these data.

In recent studies of crustaceans, ixodidae ticks, and live cells embedded in an agarose gel,[13,14] axial rotation of the specimens, enclosed in a cylindrical capillary, was demonstrated to allow confocal slicing of the sample in multiple directions; this axial
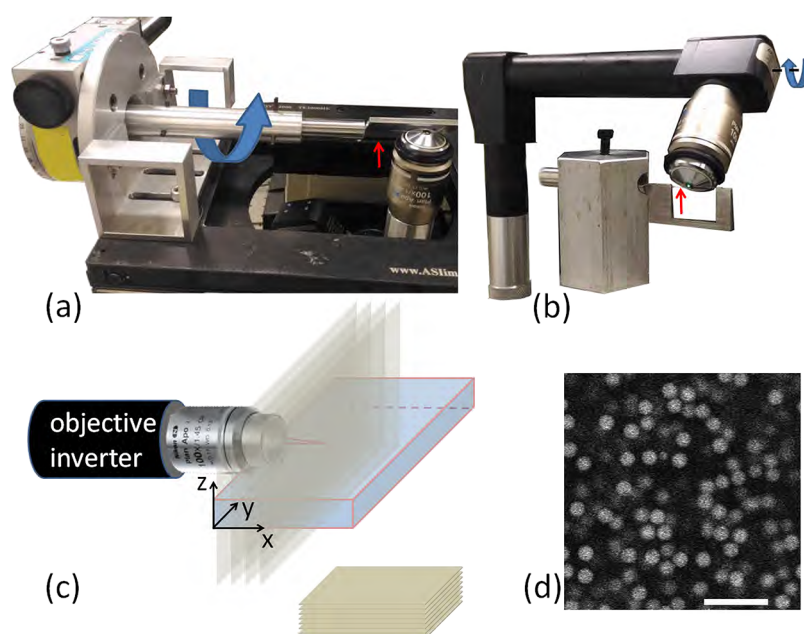
Figure 1. (a) ACT setup allowing slices in a wide range of sample orientations to be collected for rotatable samples, contained in a cylindrical capillary (marked by a red arrow). The sample is rotated about the long axis of the capillary and translated in the horizontal plane employing a combination of a rotation stage and a translation stage. The distance between the sample and the objective is controlled by the microscope nosepiece. (b) ACT of nonrotatable samples, contained in cylindrical capillaries, requires the optical axis to be rotated by an objective inverter. Here, sample translation in all three spatial dimensions is enabled, since the translation range of a typical nosepiece is too short for the ACT measurements in a wide angular range to be carried out. The sample containing capillary is marked by a red arrow. Dashes mark the rotation axis of the objective inverter. (c) For a rectangular capillary, only two different orientations of the optical axis are possible; here, the optical axis is horizontal (marked in red). The classical orientation of the confocal slices is shown at the bottom. (d) Typical confocal slice of a colloidal suspension, obtained with the optical axis aligned along the gravitational direction and along the z-axis of the rectangular capillary. Note that the particles are isotropically distributed, and no particle chains are visible. The scale bar length is 10 μm.

confocal tomography (ACT) allowed the resolution for all three spatial dimensions of the specimen to be maximized, effectively overcoming the anisotropy of the PSF.[15] A similar goal was also achieved by applying optical tweezers to rotate individual bacteria under the microscope.[16] However, ACT has never been applied yet to colloidal science. The implementation of ACT to colloids is challenged by the fact that some samples, such as colloidal sediments, cannot be rotated: rotation with respect to the direction of gravity changes their structure. Also, samples exhibiting long-range particle correlations are sensitive to the shape of the enclosing capillary; embedding these samples in a cylindrical capillary may alter their behavior. Thus, confocal reconstructions of colloidal structures are based on complex numerical algorithms;[8−12,17,18] some peculiar inaccuracies of such algorithms remain hidden for decades, in spite of their very active employment by many groups worldwide.[8,19,20] Solid testing grounds, which may be provided by ACT for such algorithms, are essential for colloidal science.

In this paper, we apply ACT to fluid suspensions and solid noncrystalline sediments of colloidal spheres. We extend the ACT method to samples which cannot be rotated and to noncylindrical capillaries. We identify the potential pitfalls of this method and demonstrate how these pitfalls may be avoided. While our work focuses on colloids, these extensions of ACT also contribute to other fields of science where specimen fixation for axial rotation is challenging. Moreover, similar methods may be applied in combination with various nanoscopy approaches,[42] such as the 2D stimulated emission depletion (STED) where the lateral resolution is reduced to <50 nm, whereas the resolution along the optical axis remains

similar to confocal microscopy.[21] Although the extension of STED into the axial direction does enable a spherical PSF,[22] the combination of 2D STED and axial tomography remains more powerful, resulting in a smaller PSF in all directions. Thus, some of the remarkable recent success of transmission electron microscopy tomography[23,24] may possibly be achieved by ACT and other similar optical tomography techniques, with the potentially destructive sample freezing/drying completely avoided and beam damages practically eliminated.

■ EXPERIMENTAL SECTION

We apply the ACT method to both apolar and polar colloidal suspensions. For the apolar (or low-polar) suspensions, we use PMMA [poly-(methylmethacrylate)] spheres, fluorescently-labeled for confocal imaging by either DiIC$_{18}$ (1,1′-dioctadecyl-3,3,3′,3′-tetramethylindo-tricarbocyanine iodide), NBD (7-nitro-1,2,3-benzoxadiazole), rhodamine B isothiocyanate, or the Nile Red dye.[2,11,19,20,25−27] To form fluid suspensions, these particles were suspended in buoyancy-matched tetrachloroethylene/decahydronaphthalene (TCE/DHN) and bromocyclohexane/ DHN mixtures, where mixed DHN was used. These mixtures roughly match the refractive index of the particles ($n_{apol} \approx 1.49$); thus, light scattering is weak, allowing the confocal imaging to be carried out at depths >100 μm into the bulk of the suspensions. A more precise index matching was achieved, where necessary, by introducing tetrahydronaphthalene into these solvent combinations[20,28,29] and replacing mixed DHN by a pure *cis*-DHN. To prepare colloidal sediments, PMMA particles were centrifuged (3000 rcf) in either a pure DHN or a DHN /tetrahydronaphthalene mixture. The dielectric constants of all the abovementioned solvent combinations are in the 2−6 range, too low for the dissolution of most common salts; thus, micron-scale Debye lengths are common.[3,29−31] The PMMA particles were sterically stabilized by

poly-(hydroxystearic)acid, which minimizes the van der Waals attractions.[25,30] Particle diameters σ ranged from 1.5 to 6 μm.

For polar suspensions, we employed the recently devised[32] poly(trifluoroethyl methacrylate-co-t-butyl methacrylate) (PTFEMA/PtBMA) colloids, fluorescently labeled with pyrromethene 546 (aka BODIPY 493; Exciton Inc. Dayton, US) and suspended in a density- and index-matching mixture of formamide and sulfolane. The dielectric constant of this mixture is $\epsilon \approx 82$, which is close to that of pure water. Sodium chloride (30 mM) was dissolved in this mixture for screening of electrostatic interactions. Two particle diameters were tested: 1.9 and 2.4 μm; the results were essentially the same for both particle sizes.

The suspensions were loaded into rectangular or cylindrical, borosilicate or fused silica VitroCom capillaries, widely used in the colloidal community and beyond, and sealed with a Devcon 5 Minute Epoxy glue. The imaging was carried out with a laser-scanning confocal fluorescence microscope (Nikon Ti-E-based A1R), exciting with $\lambda = 514$ nm and scanning in either the galvanometric or the resonant mode. Imaging with the VisiTech VT-Infinity3 multipoint-scanning microscope led to similar results. For rapid scanning along the optical axis (with either confocal setup), the objective was mounted on a PI (P-725.2CL) piezo stage. For confocal imaging of samples contained in rectangular capillaries, the capillaries were fixed at the edge of an L-shaped construction, made of two supporting glass slides. Two different orientations of the capillary with respect to the microscope sample stage are possible with such a construction. For the ACT data to be collected over a continuous range of >200°, the samples were loaded into cylindrical VitroCom borosilicate capillaries (i.d. = 0.1 mm), and the configurations shown in Figure 1a,b were used. The capillaries were mounted on a U-shaped aluminum capillary holder (shown in Figure 1b). For samples which could be rotated with respect to gravity, this holder was mounted on a D-8219 Huber rotation stage (Figure 1a), allowing the capillary to be rotated about its long axis with an accuracy of 0.01°. The rotation stage was mounted onto the MS-2000 ASI stage for horizontal translation. For full ACT of nonrotatable samples, we fixed the capillary holder directly to the horizontal translation stage, with this stage itself mounted on top of a vertical translation stage. For imaging of nonrotatable samples, contained in either the rectangular (Figure 1c) or the cylindrical (Figure 1b) capillaries, we used an InverterScope objective inverter from LSM Tech, which is a simple periscope, allowing the optical axis to be rotated in any spatial direction. The rotation axis employed in our work is marked in Figure 1b. We graduated the inverter for rotations about this axis (the current graduation allows for a resolution of 3.75°). A 100× Nikon Plan Apo VC or λ oil immersion objective (NA = 1.4 and 1.45, respectively) was mounted on top of the objective inverter (Figure 1b,c). When the optical axis is at an angle with the vertical (i.e., the scanning axis of the microscope's nosepiece), the images appear to be rotated by that angle. To eliminate this effect where necessary, we carried back-rotation by a standard ImageJ procedure.

The ray-tracing calculations, employing geometrical optics, were carried out with a dedicated MATLAB code. The wave front of the illuminating radiation is numerically approximated by $\sim 10^4$ separate rays, aiming toward a common focal point inside the sample. The rays refract, according to the Snell's law, at the external and the internal interfaces of a cylindrical capillary. We neglect multiple reflection phenomena and the dependence of the reflected and refracted intensities on the angle of incidence. The chromatic dispersion is also neglected.

■ RESULTS AND DISCUSSION

As a test case for the ACT method, we employ a fluid suspension of PMMA colloidal spheres in a density- and index-matching TCE/DHN mixture. Earlier experiments demonstrated that the bulk structures of similar suspensions are closely matched by the hard spheres' theoretical model,[2,19] indicating that the van der Waals attractions and the charge effects are very small.[30,33] Indeed, in confocal slices taken

through the wide wall of the rectangular VitroCom capillary, the suspension looks isotropic and disordered like a simple fluid of hard spheres (Figure 1d). To reconstruct the 3D structure of the fluid by one of the common classical procedures,[10] we collected a 3D stack of such slices. The slice separation was $\sim 0.1\sigma$, where σ is the particle diameter. With the particle centers in all slices located,[19] we use the fact that each particle is visible in ~ 10 different cross sections to evaluate the full 3D coordinates of its center.[10] Although more advanced algorithms, treating the positioning along all three axes equally and evaluating the PSF, have been proposed,[8,12] their implementation remains quite challenging even with the modern computer architectures. Therefore, the "linking" of particle cross sections' centers to locate its 3D center position is widely used in colloidal studies; however, the strong anisotropy of the PSF, distorting particle shapes, challenges both the linking process and its testing by comparison to the raw 3D confocal data. In particular, the tracked 3D particle centers imply that the distribution of nearest neighbors $P(\theta,\phi)$ about each particle is rotationally anisotropic, peaking along the optical axis (Figure S1). The peak-to-peak variation of $P(\theta,\phi)$ strongly depends on the details of the linking algorithm and on the involved parameter values, commonly exceeding 20%; peaks in the focal plane may occur as well, depending on the subtleties of the linking algorithm. The observed shape of $P(\theta,\phi)$ suggests z-oriented chains to be formed within these samples, breaking the fluid rotational symmetry (see Figure 1c for the geometry).

To directly test the validity of our 3D linking, we employ ACT, confocally slicing the sample with the optical axis kept parallel to the x-axis of the capillary, as shown in Figure 1c. To avoid optical refraction at the complex-shaped side walls of the VitroCom borosilicate capillaries, potentially inducing complex lensing effects, we immerse the objective in an aqueous mixture of glycerol, which closely matches the refractive index of borosilicate. As expected, the ACT images of this sample, for all cross-section orientations, are perfectly isotropic: no chain formation can be discerned (Figure 2a). Thus, the apparent anisotropy of $P(\theta,\phi)$ owes to possible inaccuracies of the 3D particle-linking procedure.

With the isotropy of our fluids confirmed by ACT, we use these fluids to improve the accuracy of the particle-linking algorithms. In particular, we noticed that an increased sensitivity of some of the 3D reconstruction algorithms to fluctuations of particle intensity between the subsequent confocal slices may occasionally result in particle double counting.[10] The duplicated particles thus produced form short chains aligned along the optical axis, giving rise to the artificial anisotropy of $P(\theta,\phi)$. This artifact is readily eliminated by neglecting intensity fluctuations below a certain threshold, demonstrating the advantage of ACT for quality control of 3D reconstructions (Figure S1). Although only homogeneously labeled colloids are used in our current work, the 3D reconstruction precision is also improved for core−shell colloids, where only the cores are fluorescent and the optically transparent shells allow for better feature separation in optical microscopy;[34] however, the synthesis of the core−shell particles is more involved. Notably, although only four different ACT slice orientations are possible for rectangular capillaries, cylindrical capillaries allow for a continuum of slice orientations, providing a great wealth of data. Thus, the parameters of 3D-linking algorithms can be fine-tuned,
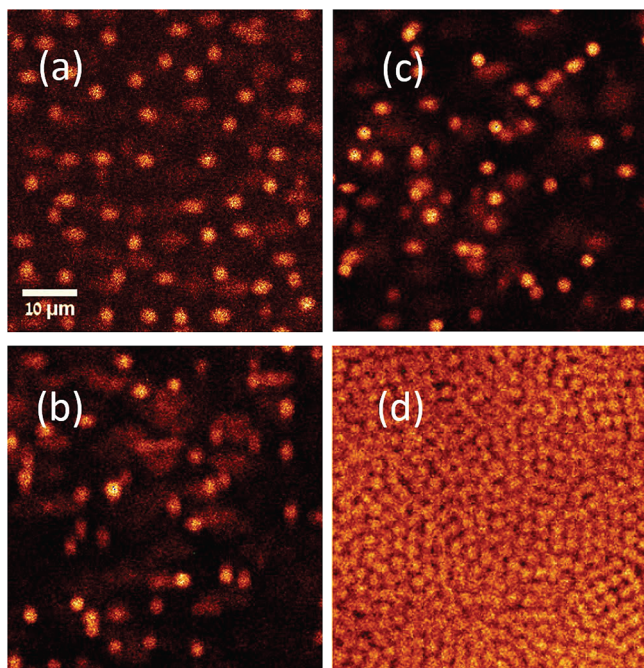
Figure 2. Vertical ACT *yz*-slices taken through the colloidal fluids allow the rotational isotropy of these systems to be confirmed, providing a benchmark for the classical 3D confocal reconstruction algorithms. (a) PMMA particles density- and index-matched in a TCE/DHN mixture. Note that this *yz*-slice through the fluid appears isotropic, akin to the *xy*-slice shown in Figure 1d. (b) To optimize the quality of the ACT images, an accurate matching of the refractive indices of all optical elements downstream of the objective is necessary, as achieved here for the PTFEMA/P*t*BMA suspension. In particular, the slight aberration-induced smearing of PMMA colloids in (a) is completely eliminated here. Changing from fused silica (b) to borosilicate (c) capillary does not strongly deteriorate the optical quality, as long as the immersion fluid is index-matched with the capillary wall. (d) For fully index-matched suspensions of PTFEMA/P*t*BMA, even the high-density solid colloidal sediments, prepared by settling in a centrifuge appear perfectly isotropic, further emphasizing the ACT capabilities.

achieving high-accuracy 3D reconstructions with either the homogeneously labeled or the core−shell particles.

A further improvement to the optical quality of the ACT slices is achieved by matching the refractive indices of all optical components. Instead of the PMMA particles ($n_{apol} \approx 1.49$), deviating in their refractive index from the VitroCom capillaries, we employ PTFEMA/P*t*BMA colloids, suspended in a mixture of formamide and sulfolane. We introduce this polar suspension into a fused silica rectangular VitroCom capillary and closely match the refractive index of both the suspension ($n_{pol} = 1.45$) and the capillary ($n_{fs} = 1.46$) by an immersion liquid composed of water and glycerol ($n_{WG} = 1.45$). The ACT images of this sample, for all cross-section orientations, are still perfectly isotropic (Figure 2b). Remarkably, the slight optical aberrations which distorted the PMMA colloids' appearance in Figure 2a do not occur for PTFEMA/P*t*BMA (Figure 2b), demonstrating the importance of having all scattering and refraction effects eliminated by index matching. Indeed, the aberrations reemerge when the fused silica capillary is replaced by a borosilicate one ($n_{bs} = 1.47$, Figure 2c).

With the scattering and refraction minimized, ACT can readily be applied to samples at much higher particle densities.

In particular, we obtain a *yz*-ACT slice through a solid random packing of PTFEMA/P*t*BMA colloids (Figure 2d), where the particle volume fraction is $\varphi \approx 0.6$;[2] note the excellent image quality. Accurate classical 3D confocal reconstructions are increasingly challenging at high φ, which further emphasizes the benefits of ACT.

Although only a few different optical axis orientations are possible with the rectangular capillaries, a wide and continuous range of such orientations is accessible for samples contained in cylindrical capillaries. For rotatable samples contained in cylindrical capillaries, we employ the setup in Figure 1a to demonstrate imaging of the same sample region over a range of different directions (Figure S2 and Video S1). For nonrotatable samples, we rotate the optical axis, while the sample is translated with no rotation (Figure 1b). Again, a wide range of imaging orientations is possible, as demonstrated in Video S2. Advanced algorithms, allowing particles to be located by processing image stacks taken from different angles of observation (through the same sample region), are currently under development. These algorithms, potentially allowing for a much greater precision in particle location, should not require tremendously large computational resources or an a priori knowledge of the PSF.[8,12]

While refractive index variation across the sample deteriorates the image quality as shown, much more dramatic artifacts occur in ACT when the refractive index of the immersion fluid mismatches that of the capillary wall. These effects are quite subtle and also occur in some other situations, where imaging through curved interfaces is involved;[35] thus, we discuss these artifacts in some detail. In particular, while the *xy*-slices through the PMMA suspensions appear isotropic (Figure 1d), a significant structuring appears in the *yz*-slices, when obtained with the type A immersion oil ($n_A = 1.52$) for suspensions contained in the borosilicate capillaries (Figure 3a). These apparent chains fluctuate and diffuse around, as demonstrated in Video S3. The chains only appear at relatively large depths into the bulk of the sample ($x > 50$ μm); closer to the capillary wall, the fluid looks much more isotropic. The chains' appearance is independent of sample orientation with respect to gravity; thus, chain formation is not a result of a (possible) small deviation from perfect neutral buoyancy. The chains exist at different φ, with the excess probability for z-aligned nearest-neighbor bonds monotonically decreasing with φ. Yet, these artificial chains are clearly visible even at an ultrahigh $\varphi \approx 0.6$ in a solid amorphous sediment[2] of these colloids (Figure 3b). This artifact is not sensitive to the particularities of the particle synthesis, appearing for different PMMA particle batches and also for colloids with a covalently linked fluorescent dye, "heat-shocked"[27] for rapid equilibration with the solvent (see Figure S3). In low-φ fluids, the intrachain particle spacing is increased (Figure 3c and Video S4). This apparent long range of intrachain particle repulsions, as also chains' alignment with respect to the capillary walls, is not an electrostatic effect, contrasting with the true physical chains formed by external AC electric fields in similar suspensions.[31,36] Indeed, the electrostatics should be tunable by colloid and solvent charge regulation, commonly achieved by the introduction of TBAC (tetrabutylammonium chloride) or AOT (dioctyl sulfosuccinate sodium surfactant) micelles into the suspension.[37−39] As expected, no systematic variation of either the artificial chain alignment or the intrachain particle spacing is detected with the introduction of AOT or TBAC at various concentrations, even when conductivities exceed 1 μS/m. The corresponding sub-
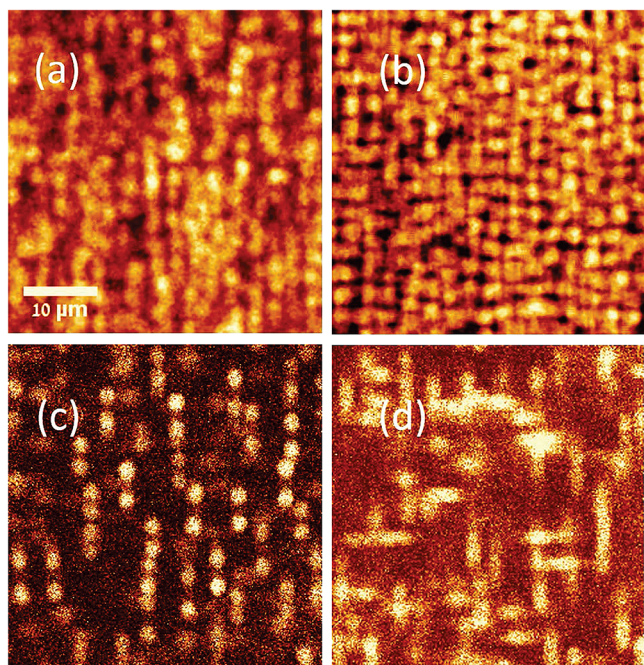
Figure 3. Artificial particle chains in "side-view" ACT images of colloidal suspensions. These confocal cross sections were obtained through the narrow (yz-)wall of the rectangular 0.1 × 2 × 50 mm borosilicate VitroCom capillaries, with the Nikon type A oil used for objective immersion. (a) Dense fluid of PMMA colloids in a density- and index-matching TCE/DHN solvent exhibits z-aligned artificial chains (see also Video S3). (b) Chains appear in solid sediments of the same particles as well. Compared to Figure 2d, where a similar sediment is shown to be completely isotropic. (c) Larger intrachain particle separations occur in dilute suspensions, as if the particles repel by electrostatics. (d) These artificial chains, born by light refraction at the walls of the capillary, are visible even for the polar suspensions, where $\epsilon \approx 82$ and significant ion concentrations are present. With the intrachain particle separations far exceeding the Debye length, chain formation cannot be attributed to the electrostatic interactions.

μm Debye lengths are much smaller than the distance between the apparent chains and the capillary walls. It is even smaller than the intrachain particle separation. Evidently, electrostatic interactions in common polar solvents cannot exceed the Debye length by so much. While the electrostatics of the *apolar* solvents at ultralow charge concentrations is not yet well-established,[38,39] similar chains are visible also in the *polar* PTFEMA/P*t*BMA suspensions, where the Debye length (at 30 mM NaCl) <2 nm is precisely known (Figure 3d).

While clearly not of an electrostatic origin, the artificial chains' alignment along the z-axis of the sample-containing capillary suggests that the container plays an important role in chain formation. Indeed, we see no chains in capillaries with square (0.5 × 0.5 and 0.6 × 0.6 mm) cross sections. Also, no chains form in a cuvette (~0.1 × 2 × 2 mm) prepared by carefully gluing together several standard fused silica or borosilicate microscopy cover slips. Because changing the objective immersion oil from type A (n_A = 1.52) to a glycerol−water mixture (n_{WG} = 1.15) eliminates the artificial structuring of the fluid (Figure 2a), we conclude that the apparent chains are resulted by a complex lensing effect along the z-axis of the rectangular VitroCom capillaries, which significantly distorts the optical image in the z-direction.

For the details of this lensing mechanism to be fully resolved, the exact shape and thickness profile of the rectangular capillary side walls must be known. This profile is not available from the manufacturer and is also challenging to measure. However, a similar artificial chain formation effect is also detected for capillaries with a rounded cross section, 0.6 mm in internal diameter, where the geometry is simpler. We trace the optical rays refracted at the 0.12 mm-thick walls of such a capillary, with the type A oil used for the objective immersion. In our case, the refraction at the capillary walls dominates optical distortions; therefore, for simplicity, we only use geometrical optics and neglect other aberration sources. Under the settings considered, for a flat 0.12 mm-thick coverslip, the optical rays emanate from the 100× objective (NA = 1.4), propagating inside the immersion fluid toward a single focal point, at a distance of 60 μm into the bulk of the suspension (n_{apol} = 1.49).
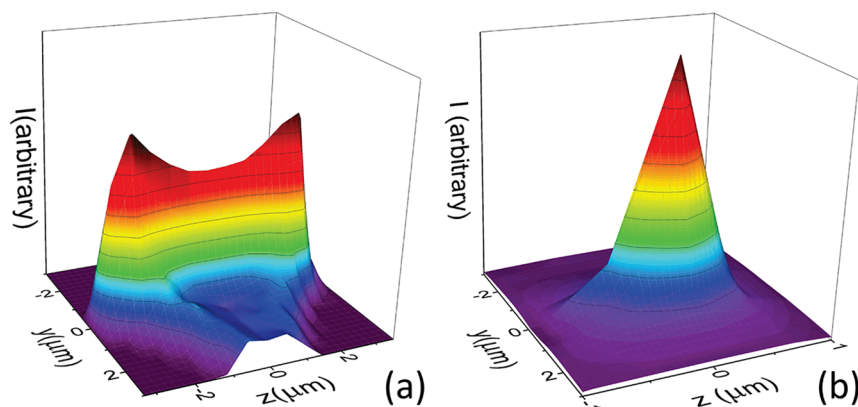

Figure 4. Ray-tracing calculations demonstrate that the curvature of side walls in cylindrical capillaries gives rise to a splitting of the focal point. (a) Rays emanating from the objective toward a single focal point at a depth of 60 μm, refract at the capillary wall. As a result, the rays split in two groups, each of which intersects at a different location, giving rise to splitting of the focus. The two peaks of the intensity I correspond to the locations of the two foci in a yz-cross section of the sample, 56 μm from the capillary wall. Here, the refractive index of the suspension is n_{apol} = 1.49, and the type A (n_A = 1.52) immersion oil is used with fused silica capillaries. (b) Repeating the same calculation with the type A immersion oil replaced by a glycerol/water mixture (n_{WG} = 1.45) yields only a single focus (at a depth of 64 μm); thus, no artificial chains are expected to form. This prediction is fully corroborated by experiment (Figure 2). Note that the different z scale in (a) and (b) further emphasizes the sharpness of the single focal point as shown in (b).

However, when the coverslip is replaced by a rounded capillary wall, the rays do not intersect at an individual location inside the sample. Instead, two separate focal points are clearly visible, as demonstrated in Figure 4a. The duplication of foci along the z-axis of the capillary (Figure 1c) gives rise to an artificial formation of z-oriented particle pairs, as shown in Figure 3c: each such pair is simply a duplicated image of an individual particle. The focal points are separated by ∼4 μm, in a good agreement with the experimentally detected intrachain particle spacing. A similar phenomenon has been very recently detected in light-sheet microscopy images of very dilute colloids ($\varphi \rightarrow 0$), enclosed in cylindrical capillaries.[40]

To experimentally confirm that the particle chains are formed by an artifactual multiplication of individual particle images, we prepare a binary mixture of PMMA particles of two different sizes. An artificial chain formed by optical image multiplication must ultimately consist of one particle size only: no mixed chains of small and large particles can form by this mechanism. This prediction is fully corroborated by our experiment. All experimentally detected chains consist of only one type of particles: no mixed chains are observed (see Video S5). This experiment provides clear-cut evidence that the chains are formed by an optical artifact, which is in agreement with our ray tracing. In addition, we also confirm this result by particle counting: average particle densities in the yz-slices obtained through the side wall of the rectangular capillaries are higher than in the xy-slices, obtained through the bottom.

To completely avoid the optical ACT artifacts discussed above, the refractive indices of all components of the optical path must be matched. Ideally, the refractive index of the objective should be matched to the other components as well. In particular, a glycerol objective, equipped by a correction ring to compensate for index variations between 1.447 and 1.455, is commercially available and may be used for the PTFEMA/PtBMA system, as also for silica colloids (see Figure S4). Clearly, such matching is impossible for most samples and in particular where the studied specimens are natural, rather than synthetic. However, our ray-tracing calculations demonstrate that the refraction-induced splitting of foci may be eliminated, once the refractive index of the immersion fluid matches that of the capillary wall. For example, for the apolar PMMA suspension, replacing the type A immersion fluid by the capillary-matching glycerol/water mixture eliminates focal splitting, in spite of the refractive index of this suspension $n_{apol} = 1.49$ being mismatched with other components of the optical path (cf. Figure 4a,b). Other types of aberration may be present in such index-mismatched optical configurations, but usually these are less dramatic than the formation of particle chains. Indeed, replacing the immersion fluid in our experimental ACT of apolar PMMA suspensions completely eliminated the artificial chains (cf. Figures 2a and 3c), as predicted by ray-tracing calculations.

CONCLUSIONS

In ACT, the orientation of the confocal PSF is varied relative to the sample, so that the highest optical resolution is achieved in all three dimensions. We have realized ACT with colloidal samples in a wide range of particle densities. The necessary measures to avoid the optical artifacts in such experiments were thoroughly discussed. In particular, index-matching of the curved capillary walls by immersion liquid was shown to be crucial, for the artifactual duplication of particle images to be avoided. We have demonstrated ACT to set a benchmark for

testing of the 3D reconstruction algorithms, allowing their accuracy and reliability to be significantly improved. In the future, the demonstrated ACT of samples slowly rotated in cylindrical capillaries may also be used to approximate decreased-gravity conditions, of current interest to the colloidal community and beyond.[41]

ASSOCIATED CONTENT

Ⓢ Supporting Information

The Supporting Information is available free of charge on the ACS Publications website at DOI: 10.1021/acs.langmuir.7b03039.

> Description of the video files; anisotropy and isotropy of angular nearest neighbor distribution $P(\theta,\phi)$; collage of ACT cross sections taken through the same region of a dense colloidal sample; artificial particle chains in side-view ACT images of 'heat-shocked' PMMA colloids; and imaging with a fully index-matched setup (PDF)
> ACT imaging, over a continuous angular range, by sample rotation (AVI)
> ACT imaging, over a continuous angular range, by rotation of the optical axis (AVI)
> Dynamics of artificial chains at high ϕ (AVI)
> Dynamics of artificial chains at low ϕ (AVI)
> The absence of mixed particle chains in binary colloidal mixtures demonstrates that the chains are an optical artifact (AVI)

AUTHOR INFORMATION

Corresponding Author
*E-mail: eli.sloutskin@biu.ac.il.

ORCID Ⓞ
Ernest B. van der Wee: 0000-0002-0139-4019
Peter J. Lu: 0000-0003-1489-5725
David A. Weitz: 0000-0001-6678-5208
Eli Sloutskin: 0000-0002-7109-6893

Author Contributions
S.R.L. and G.I. contributed equally to this work.

Notes
The authors declare no competing financial interest.

REFERENCES

(1) Conchello, J.-A.; Lichtman, J. W. Optical Sectioning Microscopy. *Nat. Methods* **2005**, 2, 920−931.
(2) Liber, S. R.; Borohovich, S.; Butenko, A. V.; Schofield, A. B.; Sloutskin, E. Dense Colloidal Fluids Form Denser Amorphous Sediments. *Proc. Natl. Acad. Sci. U.S.A.* **2013**, 110, 5769−5773.

(3) Cohen, A. P.; Dorosz, S.; Schofield, A. B.; Schilling, T.; Sloutskin, E. Structural Transition in a Fluid of Spheroids: A Low-Density Vestige of Jamming. *Phys. Rev. Lett.* **2016**, *116*, 098001.

(4) Kuijk, A.; Imhof, A.; Verkuijlen, M. H. W.; Besseling, T. H.; van Eck, E. R. H.; van Blaaderen, A. Colloidal Silica Rods: Material Properties and Fluorescent Labeling. *Part. Part. Syst. Charact.* **2014**, *31*, 706−713.

(5) Besseling, T. H.; Hermes, M.; Kuijk, A.; de Nijs, B.; Deng, T.-S.; Dijkstra, M.; Imhof, A.; van Blaaderen, A. Determination of the Positions and Orientations of Concentrated Rod-Like Colloids from 3D Microscopy Data. *J. Phys.: Condens. Matter* **2015**, *27*, 194109.

(6) Guttman, S.; Sapir, Z.; Schultz, M.; Butenko, A. V.; Ocko, B. M.; Deutsch, M.; Sloutskin, E. How Faceted Liquid Droplets Grow Tails. *Proc. Natl. Acad. Sci. U.S.A.* **2016**, *113*, 493−496.

(7) Besseling, T. H.; Jose, J.; van Blaaderen, A. Methods to Calibrate and Scale Axial Distances in Confocal Microscopy as a Function of Refractive Index. *J. Microsc.* **2015**, *257*, 142−150.

(8) Leocmach, M.; Tanaka, H. A Novel Particle Tracking Method with Individual Particle Size Measurement and its Application to Ordering in Glassy Hard Sphere Colloids. *Soft Matter* **2013**, *9*, 1447−1457.

(9) van Blaaderen, A.; Wiltzius, P. Real-Space Structure of Colloidal Hard-Sphere Glasses. *Science* **1995**, *270*, 1177−1179.

(10) Lu, P. J.; Sims, P. A.; Oki, H.; Macarthur, J. B.; Weitz, D. A. Target-Locking Acquisition with Real-Time Confocal (TARC) Microscopy. *Opt. Express* **2007**, *15*, 8702−8712.

(11) Dinsmore, A. D.; Weeks, E. R.; Prasad, V.; Levitt, A. C.; Weitz, D. A. Three-Dimensional Confocal Microscopy of Colloids. *Appl. Opt.* **2001**, *40*, 4152−4159.

(12) Bierbaum, M.; Leahy, B. D.; Alemi, A. A.; Cohen, I.; Sethna, J. P. Light Microscopy at Maximal Precision. **2017**, arXiv:1702.07336 [cond-mat.soft].

(13) Bruns, T.; Schickinger, S.; Schneckenburger, H. Sample Holder for Axial Rotation of Specimens in 3D Microscopy. *J. Microsc.* **2015**, *260*, 30−36.

(14) Richter, V.; Bruns, S.; Bruns, T.; Weber, P.; Wagner, M.; Cremer, C.; Schneckenburger, H. Axial Tomography in Live Cell Laser Microscopy. *J. Biomed. Opt.* **2017**, *22*, 091505.

(15) Heintzmann, R.; Cremer, C. Axial Tomographic Confocal Fluorescence Microscopy. *J. Microsc.* **2002**, *206*, 7−23.

(16) Carmon, G.; Kumar, P.; Feingold, M. Optical Tweezers Assisted Imaging of the Z-Ring in *Escherichia Coli*: Measuring Its Radial Width. *New J. Phys.* **2014**, *16*, 013043.

(17) Crocker, J. C.; Grier, D. J. Methods of Digital Video Microscopy for Colloidal Studies. *J. Colloid Interface Sci.* **1996**, *179*, 298−310.

(18) Dassanayake, U.; Fraden, S.; van Blaaderen, A. Structure of Electrorheological Fluids. *J. Chem. Phys.* **2000**, *112*, 3851−3858.

(19) Lu, P. J.; Shutman, M.; Sloutskin, E.; Butenko, A. V. Locating Particles Accurately in Microscope Images Requires Image-Processing Kernels to be Rotationally Symmetric. *Opt. Express* **2013**, *21*, 30755−30763.

(20) Gao, Y.; Kilfoil, M. L. Accurate Detection and Complete Tracking of Large Populations of Features in Three Dimensions. *Opt. Express* **2009**, *17*, 4685−4704.

(21) Wildanger, D.; Medda, R.; Kastrup, L.; Hell, S. W. A Compact STED Microscope Providing 3D Nanoscale Resolution. *J. Microsc.* **2009**, *236*, 35−43.

(22) Klar, T. A.; Jakobs, S.; Dyba, M.; Egner, A.; Hell, S. W. Fluorescence Microscopy with Diffraction Resolution Barrier Broken by Stimulated Emission. *Proc. Natl. Acad. Sci. U.S.A.* **2000**, *97*, 8206−8210.

(23) de Nijs, B.; Dussi, S.; Smallenburg, F.; Meeldijk, J. D.; Groenendijk, D. J.; Filion, L.; Imhof, A.; van Blaaderen, A.; Dijkstra, M. Entropy-Driven Formation of Large Icosahedral Colloidal Clusters by Spherical Confinement. *Nat. Mater.* **2015**, *14*, 56−60.

(24) Zanaga, D.; Bleichrodt, F.; Altantzis, T.; Winckelmans, N.; Palenstijn, W. J.; Sijbers, J.; de Nijs, B.; van Huis, M. A.; Sánchez-Iglesias, A.; Liz-Marzán, L. M.; van Blaaderen, A.; Batenburg, K. J.; Bals, S.; van Tendeloo, G. Quantitative 3D Analysis of Huge Nanoparticle Assemblies. *Nanoscale* **2016**, *8*, 292−299.

(25) Antl, L.; Goodwin, J. W.; Hill, R. D.; Ottewill, R. H.; Owens, S. M.; Papworth, S.; Waters, J. A. The Preparation of Poly(methyl Methacrylate) Latices in Non-Aqueous Media. *Colloids Surf.* **1986**, *17*, 67−78.

(26) Cohen, A. P.; Alesker, M.; Schofield, A. B.; Zitoun, D.; Sloutskin, E. Photo-Crosslinkable Colloids: From Fluid Structure and Dynamics of Spheres to Suspensions of Ellipsoids. *Gels* **2016**, *2*, 29.

(27) Kodger, T. E.; Lu, P. J.; Wiseman, G. R.; Weitz, D. A. Stable, Fluorescent Polymethylmethacrylate Particles for the Long-Term Observation of Slow Colloidal Dynamics. *Langmuir* **2017**, *33*, 6382−6389.

(28) Wiederseiner, S.; Andreini, N.; Epely-Chauvin, G.; Ancey, C. Refractive-Index and Density Matching in Concentrated Particle Suspensions: a Review. *Exp. Fluids* **2011**, *50*, 1183−1206.

(29) Cohen, A. P.; Janai, E.; Mogilko, E.; Schofield, A. B.; Sloutskin, E. Fluid Suspensions of Colloidal Ellipsoids: Direct Structural Measurements. *Phys. Rev. Lett.* **2011**, *107*, 238301.

(30) Royall, C. P.; Poon, W. C. K.; Weeks, E. R. In Search of Colloidal Hard Spheres. *Soft Matter* **2013**, *9*, 17−27.

(31) Yethiraj, A.; van Blaaderen, A. A Colloidal Model System with an Interaction Tunable From Hard Sphere to Soft and Dipolar. *Nature* **2003**, *421*, 513−517.

(32) Kodger, T. E.; Guerra, R. E.; Sprakel, J. Precise Colloids with Tunable Interactions for Confocal Microscopy. *Sci. Rep.* **2015**, *5*, 14635.

(33) Janai, E.; Cohen, A. P.; Butenko, A. V.; Schofield, A. B.; Schultz, M.; Sloutskin, E. Dipolar Colloids in Apolar Media: Direct Microscopy of Two-Dimensional Suspensions. *Sci. Rep.* **2016**, *6*, 28578.

(34) Klein, M. K.; Saenger, N. R.; Schuetter, S.; Pfleiderer, P.; Zumbusch, A. Shape-Tunable Core-Shell Microparticles. *Langmuir* **2014**, *30*, 12457−12464.

(35) Elbers, N. A.; van der Hoeven, J. E. S.; de Winter, D. A. M.; Schneijdenberg, C. T. W. M.; van der Linden, M. N.; Filion, L.; van Blaaderen, A. Repulsive van der Waals Forces Enable Pickering Emulsions with Non-Touching Colloids. *Soft Matter* **2016**, *12*, 7265−7272.

(36) Crassous, J. J.; Mihut, A. M.; Wernersson, E.; Pfleiderer, P.; Vermant, J.; Linse, P.; Schurtenberger, P. Field-Induced Assembly of Colloidal Ellipsoids into Well-Defined Microtubules. *Nat. Commun.* **2014**, *5*, 5516.

(37) Hsu, M. F.; Dufresne, E. R.; Weitz, D. A. Charge Stabilization in Nonpolar Solvents. *Langmuir* **2005**, *21*, 4881−4887.

(38) Smith, G. N.; Eastoe, J. Controlling Colloid Charge in Nonpolar Liquids with Surfactants. *Phys. Chem. Chem. Phys.* **2013**, *15*, 424−439.

(39) Kemp, R.; Sanchez, R.; Mutch, K. J.; Bartlett, P. Nanoparticle Charge Control in Nonpolar Liquids: Insights from Small-Angle Neutron Scattering and Microelectrophoresis. *Langmuir* **2010**, *26*, 6967−6976.

(40) Meinert, T.; Gutwein, B. A.; Rohrbach, A. Light-Sheet Microscopy in a Glass Capillary: Feedback Holographic Control for Illumination Beam Correction. *Opt. Lett.* **2017**, *42*, 350−353.

(41) El Masri, D.; Vissers, T.; Badaire, S.; Stiefelhagen, J. C. P.; Vutukuri, H. R.; Helfferich, P.; Zhang, T. H.; Kegel, W. K.; Imhof, A.; van Blaaderen, A. A Qualitative Confocal Microscopy Study on a Range of Colloidal Processes by Simulating Microgravity Conditions through Slow Rotations. *Soft Matter* **2012**, *8*, 6979−6990.

(42) Wagner, O.; Schultz, M.; Ramon, Y.; Sloutskin, E.; Zalevsky, Z. Optical-tweezing-based linear-optics nanoscopy. *Opt. Express* **2016**, *24*, 8013.